,

Instabilities and Taylor dispersion in isothermal binary thin fluid films

Z. Borden

Franklin W. Olin College of Engineering, Needham, MA

H. Grandjean

Ecole Polytechnique, Palaiseau Cedex, France

A.E. Hosoi

Hatsopoulos Microfluids Laboratory,

Massachusetts Institute of Technology, Cambridge, MA

L. Kondic

Department of Mathematical Sciences

Center for Applied Mathematics and Statistics

New Jersey Institute of Technology, Newark, NJ

B.S. Tilley*

Franklin W. Olin College of Engineering, Needham, MA

* Author to whom all correspondence should be addressed.

Abstract

Experiments with glycerol-water thin films flowing down an inclined plane reveal a localized instability that is primarily three dimensional. These transient structures, referred to as "dimples", appear initially as nearly isotropic depressions on the interface. A linear stability analysis of a binary mixture model in which barodiffusive effects dominate over the thermophoresis (i.e. the Soret effect) reveals unstable modes when the components of the mixture have different bulk densities and surface tensions. This instability occurs when Fickian diffusion and Taylor dispersion effects are small, and is driven by solutalcapillary stresses arising from gradients in concentration of one component, across the depth of the film. Qualitative comparision between the experiments and the linear stability results over a wide range of parameters is presented.

Keywords: Taylor dispersion, barodiffusion, thin films

FIG. 1: Several experimental images showing variation in dimple size. Images are ordered from left to right with 5 second intervals between each frame. The water volume fraction is $\phi = 0.3$, and the inclination angle is $\alpha = 20°$.

I. INTRODUCTION

Beginning with the fundamental experiments of Kapitza and Kaptiza ([1, 2]), interfacial phenomena on thin falling liquid films have continually inspired scientific curiosity (see *e.g.* [3–5], and more recently [6, 7]). The progression of traveling-wave solutions, uniform in the spanwise direction but unstable to long-wave three-dimensional disturbances, has been investigated experimentally using mixtures [3–5]. Mixtures provide a convenient way to vary the material properties of the film and to understand how pattern formation depends on these properties. However, the majority of these experiments are conducted either along a vertical plane, or are driven by a weak hydrostatic jump near the inlet. Furthermore, the mixture is generally expected to be well-mixed so that gradients in material properties, such as surface tension, are absent.

Binary mixtures have been of interest for many years. Starting from the formulations of Eckhart in 1940 [10], Cahn and Hilliard [11] used a binary mixture formulation along with the Korteweg tensor to model excess pressure effects in diffuse interfaces. The modern study of binary mixtures begins with the model provided by Landau and Lifshitz [15]. Here, the authors propose that the mass flux of the solute depends not only on Fickian diffusion, but also on temperature and pressure gradients. The sensitivity of mass transport to temperature differences has been well established, but its dependence on pressure differences has not been, to the best of our knowledge, well demonstrated.

The presence of flow significantly modifies the rate of diffusion of a solute within a solvent. The phenomenon of Taylor dispersion (see Taylor [16, 17]) was originally found in the

diffusion of solute in a solution flowing through a thin tube. If the flow profile is the same as Hagen-Poiseuille flow, Taylor discovered that the disturbance concentration of the solute in the solution behaves according to a modified diffusion equation

$$C_t = \left\{ \frac{1}{Pe} + \frac{Pe}{192} \right\} C_{xx} \ ,$$

where x is a frame of reference moving with the average flow velocity and Pe is the Peclet number of the solution. The first term is the modified diffusion coefficient corresponding to classical Fickian diffusion, while the latter measures the dispersion of the solute due to the advection in the flow. This result led to the efficient measurement of the diffusion coefficient between solutes and solvents [18]. We note that, although Fickian processes are isotropic, dispersion of solute in a solvent due to Taylor dispersion acts only in the direction of the flow.

Interest in model representations of binary mixtures grew in the 1990's. Joseph first proposed the notion of quasi-incompressibility in binary mixtures whose components have different bulk densities [19]. Extensions of this model appeared contemporaneously by Anderson *et. al.* [20] and Lowengrub and Truskinovsky [21] who focused on the development of interfacial theories proposed initially in [11]. Additional studies of binary mixtures include [12–14, 23, 29]. This potentially bewildering array of models is made possible by the fact that multiple mathematical formulations both conserve energy and ensure that entropy strictly increases.

The focus of current research in this field relates to temperature-driven segregation of mixtures, called thermophoresis or the Soret effect. This effect couples the mass transport and thermal transport of the fluid. Some recent examples of work in this area center on Marangoni-Rayleigh-Bénard convection [25–28] and the impact of these effects in modeling the behavior of nanofluids [8]. However, considerably less attention has been dedicated to isothermal instabilities of binary mixtures.

Figure 1 shows a series of photos illustrating the novel instability addressed herein. As the fluid flows down the incline (from top to bottom in each frame), we observe the formation of "dimples": three-dimensional instabilities that appear *ab initio* in binary mixtures. The details of the experiments are described in Section II. Section III describes the lubrication model based on the approach by Lowengrub and Truskinovsky [21] which results in two coupled evolution equations for the film in the zero Reynolds number limit, describing the

interfacial evolution and the local mean concentration of one fluid component. Section IV presents a linear stability analysis of this model, and describes the instability in terms of the product of a barodiffusion coefficient, a difference in specific volume, and a Marangoni number. We discuss the conditions under which this instability may be present, along with the dependence of the wavenumber of the most dangerous mode on inclination angle and Peclet number. Predictions of this model are consistent with reported experimental results. This comparison is discussed in our Conclusions section.

II. EXPERIMENT

Figure 2 shows a schematic of the flow apparatus. A mixture of glycerol and water is manually loaded into the upper reservoir to a specified height H. It is then driven by gravity through a 3 cm long channel underneath a gate, adjustable from 0 to 1 cm in height, and emerges onto a film plane 100 cm long and 10 cm wide. The experimental apparatus is supported by two ring stands which adjust the plate to an inclination angle α. For all experimental data presented here, the gate height was set to 0.5 mm [31]. An experimental run consists of filling the upper reservoir to a height of 8 cm and allowing the fluid to drain to a height of 2 cm. We note that, in a series of preliminary experiments, we used a pump to transport the mixture from the drainage tank back into the source tank at the top of the inclined region to maintain a constant pressure head. The fluid, however, acquired debris from the pump over time and the level of particulation appeared to be important in the onset of the observed instability. Furthermore, the pump was found to heat the fluid, establishing temperature gradients in the mixture. In order to avoid these effects, we removed the pump and simplified the experiment to the one shown in Figure 2.

To record the global thickness profile of the film over time, we utilize a fluorescence imaging system developed by Liu and Gollub [3]. The mixture consisted of water and Acros Organic 99% synthetic glycerol. The fluid is then doped with a small concentration of fluorescein ($\frac{1}{16}$ g/L) which fluoresces under ultraviolet illumination. The composition of the mixture is defined by water volume fraction which varies from $\phi = 0$ to $\phi = 1$. The water and glycerol were stirred using a magnetic stir until all fluorescein was dissolved and no concentration gradients were visually detectable. Solutions stored for longer than a few hours were remixed before use. The respective physical properties are shown in Table I. For

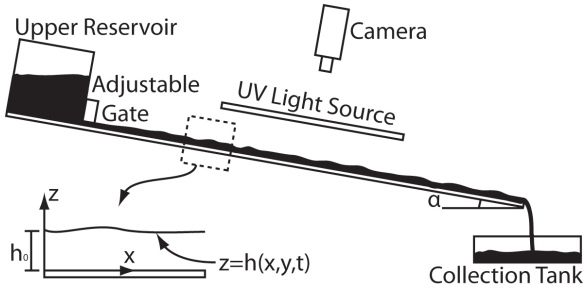

FIG. 2: Schematic diagram of the falling thin film flow apparatus with variable inclination angle α, showing the manually variable gate used to control film height and the measurement method based on fluorescent imaging.

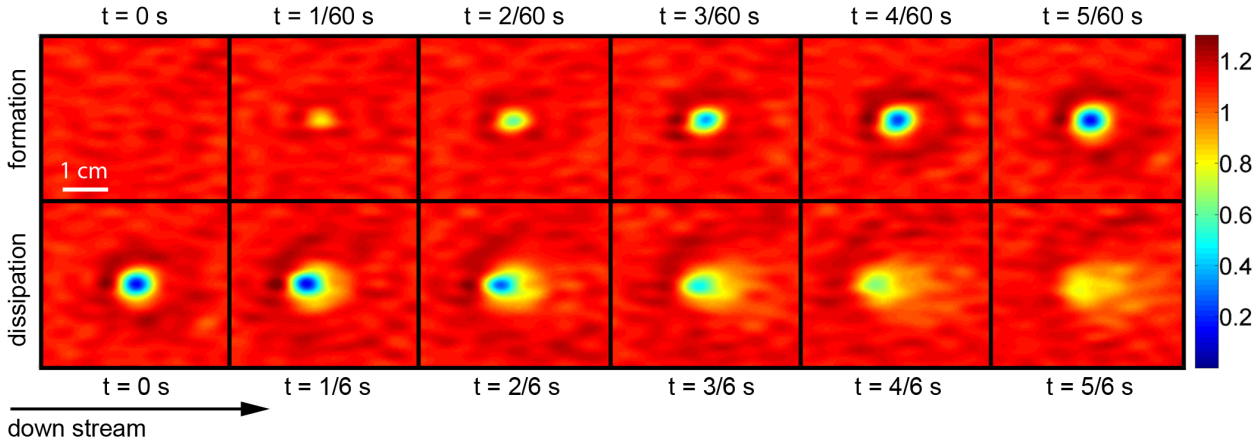

FIG. 3: (Top) Three dimensional profile of a typical dimple during formation at 1/60 second intervals for $\alpha = 20°$ and $\phi = 0.4$. Notice the dimple's 1:1 length to width aspect ratio. (Bottom) Three dimensional profile of a typical dimple during relaxation at 1/6 second intervals for $\alpha = 20°$ and $\phi = 0.4$. The aspect ratio deformation is due to flow advection. Colors indicate films thickness. The color bar units are in millimeters.

sufficiently thin films (1 mm or thinner), we find a linear relationship between intensity and height given by

$$I(x, y, t) = KI_0(x, y)h(x, y, t) \tag{1}$$

where $I_0(x, y)$ describes the illumination field as a function of UV source positioning and K is a constant. The function $I_0(x, y)$ is measured for a stable film. To determine K, a vessel with known cross-sectional area is filled with known volumes of fluid and imaged.

After a flowing film is established on the inclined plane, small transient localized depressions were observed scattered across the film surface. These depressions, referred to as

	Water ($\phi = 1$)	Glycerol ($\phi = 0$)
Density	$\rho_w = 1$ g/cm^3	$\rho_g = 1.2$ g/cm^3
Surface Tension	$\gamma_g = 64$ dynes/cm	$\gamma_w = 72$ dynes/cm
Viscosity	$\mu_w = 0.89$ cP	$\mu_g = 934$ cP

TABLE I: Physical properties of pure substances used in the mixture. $\phi = 0$ corresponds to pure glycerol and $\phi = 1$ to pure water.

"dimples," are reminiscent of the surface of a puddle during a rainstorm (see figure 1) with the exception that no driving mechanism (such as raindrops) is readily evident. Figure 3 shows the results of fluorescence imaging of individual dimples. The figure reveals that the initial shape of the dimple is conical with a length to width aspect ratio of about 2:1. This aspect ratio changes rapidly during its nonlinear evolution, and is slightly modified by advection during relaxation. High speed imaging shows that formation occurs on a timescale approximately ten times slower than relaxation. The interfacial profile in the plane along the centerline of the dimple is shown in Figure 4. From this figure, the oscillations that appear before and after the dimple formation reflect the error in our experimental technique.

Observed dimples range in size from 1 to 20 mm in diameter and exist for approximately 0.1 to 1.5 seconds. Due to limitations of the optical equipment, we are not able to resolve dimples smaller than 3 mm in diameter The variation in size is roughly illustrated in Figure 1 which shows photos of the distribution of dimples in several images from one experimental run.

In Figure 5, we show the locations of dimple formation over the entire pitch of the plate for 10 experimental runs. The majority of dimples appear near the gate region. The slight increase in dimple concentration at the bottom of this image is due to improved resolution near the lower portion of the graph and reflects the location of the light source. Notice, however, that the dimples do not preferably form at any particular location, suggesting that plate imperfections are not a driving factor in dimple formation.

Dimples were only observed in binary mixtures – they were not observed in experimental trials involving pure water or pure glycerol. In order to understand the influence of the water volume fraction on the frequency of dimpling, several experiments were carried out

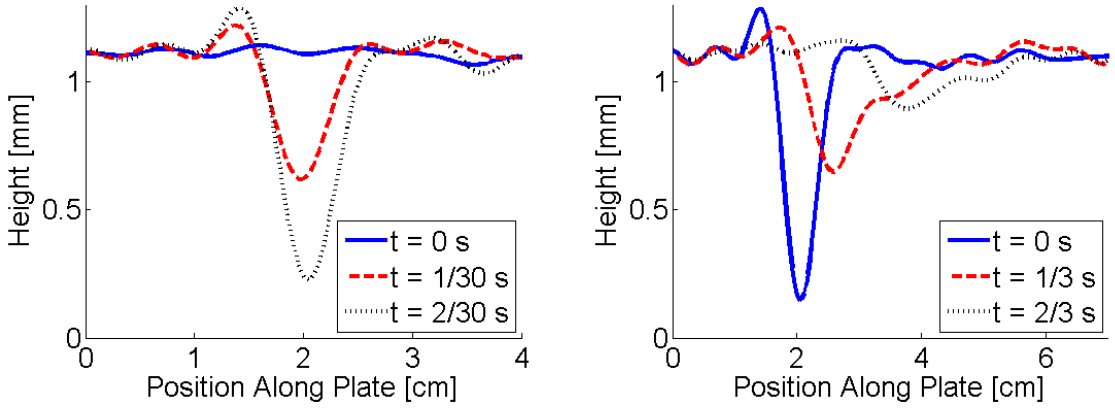

(a) (b)

FIG. 4: (a) Experimentally measured cross-sectional profile of a typical dimple during formation at 1/30 second intervals for $\alpha = 20°$ and $\phi = 0.4$ (b) Two dimensional profile of same dimple during dissipation at 1/3 second intervals. Lateral peak movement is due to flow advection.

using solutions characterized by water volume fractions of $\phi = 0.4$, $\phi = 0.5$ and $\phi = 0.6$. It is important to note that a change in ϕ simultaneously affects the concentration, viscosity, surface tension, and density of the mixture.

Several experimental trials were conducted to rule out potential mechanisms for dimple formation. We considered the possibility that shear forces in the film were causing a buildup of charge in the fluid itself or on the substrate. Such nonuniform charge distributions could lead to local deformations of the interface. However, when the channel and the collection reservoir were coated with a conductive material and grounded, dimples were still observed. We also observe a random distribution of the dimples across the plate, suggesting that liquid-solid interaction energy (and its spatial dependence on local inhomogeneities in the substrate) is not a source of instability. Finally, the film thicknesses at which dimples are observed (on the order of a millimeter) are orders of magnitude too thick for van der Waals forces to be significant.

Finally, the frequency of dimples appears to depend on the flow rate of the film. As the reservoir drains, the rate of the appearence of this instability appears to decrease with the flow rate. This suggests that the presence of a sufficient flow field is important in the development of these structures

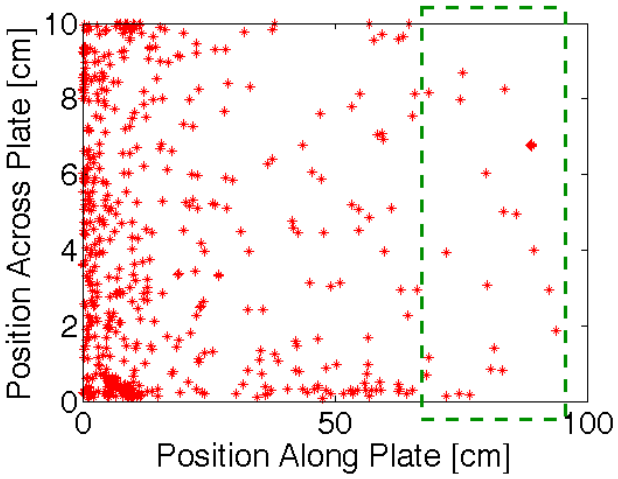

FIG. 5: Spatial locations of dimple formations over ten four-minute runs. The dashed region is the focus of our linear stability analysis.

III. LUBRICATION MODEL

In light of the fact that a binary mixture is required to drive the instability and the lack of any significant temperature gradients in our system, we propose a model that includes the effects of pressure gradients in the mass transport of solute. This effect, called barodiffusion by Landau & Lifschiz [15], is usually masked by the Soret effect when temperature fluctuations are present. The effect is pertinent when the densities of the component fluids are different (see [19–21]). Hydrostatic pressure within the film triggers this barodiffusive effect and establishes a concentration gradient normal to the inclined plane. If one of the components contains surface active agents, then these concentration gradients can lead to surface-tension gradients in the film. In this work, we show that instabilities occur when the stabilizing effects of Fickian diffusion and Taylor dispersion are small, and that the instability is primarily three-dimensional. We anticipate that the critical requirement for this instability to occur is the presence of a vertical concentration gradient of the component fluids. Barodiffusion, used here, is one potential mechanisms that can be exploited to create such a gradient, but other mechanisms (such as evaporation [22]) may be possible.

Consider the motion of an isothermal thin liquid film of a two component fluid flowing down an inclined plane. The components have different bulk densities, ρ_1, ρ_2 and different surface tensions in their pure phases, γ_1, γ_2. To compare the results of our model with the

experiment, we associate quantities with subscript 1 with glycerol and those with 2 with the bulk values for water. We note that if we have a particular mass fraction of glycerol C in the mixture then we can represent the density as

$$\frac{1}{\rho} = \frac{1}{\rho_1}C + \frac{1}{\rho_2}(1-C) \ .$$

In the following, the kinematic viscosity of the mixture is determined by the relation found in [9]

$$\ln \nu = X \ln \nu_w + (1-X) \ln \nu_g + G\, X\, (1-X) \ , \tag{2}$$

where X is the molar fraction of water and G is an empirically determined parameter.

Finally, we assume that the surface tension can be written in the form

$$\gamma(C) = \gamma_1 + (\gamma_2 - \gamma_1)(1-C) \ .$$

Note that in the experiment, surface reagents are known to exist in the manufacture of glycerol. These reagents remain attached to the glycerol proper, and need not be modeled separately from the distribution of glycerol. The presence of these reagents would simply change the value of γ_1 in our expression for surface tension.

To model conservation of mass, momentum, and water mass fraction, we use the expressions found in Lowengrub and Truskinovsky [21]:

$$\rho \frac{DC}{Dt} = \frac{\rho_1 \rho_2}{\rho_2 - \rho_1} \nabla \cdot \mathbf{u} \tag{3}$$

$$\rho \frac{D\mathbf{u}}{Dt} = -\nabla p + \rho \mathbf{g} + \nabla \cdot \left\{ \mu \left(\nabla \mathbf{u} + \nabla \mathbf{u}^T \right) \right\} \ , \tag{4}$$

$$\rho \frac{DC}{Dt} = -\nabla \cdot \mathbf{J} \ , \tag{5}$$

where $\mathbf{u} = (u, w)$ is the fluid velocity of the mixture, $\mathbf{g}$ is the gravitational vector, and μ is the dynamic viscosity of the mixture which depends on the local concentration. The first two equations represent conservation of mass and momentum, respectively, of the mixture; the final equation reflects mass conservation for one of the components. The mass flux $\mathbf{J}$ depends on solutal diffusion of the water and on the local pressure variation

$$\mathbf{J} = -\rho D \left\{ \nabla C - \frac{1}{P_o} \left(\frac{1}{\rho} \frac{\partial \rho}{\partial C} \left[\nabla p \right] \right) \right\} \ , \tag{6}$$

where P_o is the ambient pressure. The coefficient in front of the pressure gradient in (6) is called the *barodiffusion coefficient* [15]). $D \approx 10^{-4}\mathrm{cm}^2/\mathrm{s}$ is the diffusion coefficient for water in glycerol.

Along the plate, the no-slip boundary condition is applied along with no mass flux: $\mathbf{u} = 0$, $\mathbf{J}\cdot\mathbf{k} = 0$ at $z = 0$. At the free surface $z = h(x,t)$, we assume that the kinematic boundary condition applies, shear stress along the film is balanced by surface tension gradients, normal stress is balanced by capillary forces, and there is no mass flux across the interface

$$h_t + uh_x - w = 0 \tag{7}$$

$$\mathbf{t}\cdot\mathbf{T}\cdot\mathbf{n} = \nabla\gamma\cdot\mathbf{t} \tag{8}$$

$$\mathbf{n}\cdot\mathbf{T}\cdot\mathbf{n} = \gamma\kappa \tag{9}$$

$$\mathbf{J}\cdot\mathbf{n} = 0\ , \tag{10}$$

where $\mathbf{T}$ is the stress tensor

$$\mathbf{T} = -\left(p + \frac{2}{3}\mu\nabla\cdot\mathbf{u}\right)\mathbf{I} + \mu\left(\nabla\mathbf{u} + \nabla\mathbf{u}^T\right)\ .$$

We apply the following scales to nondimensionalize the system near the mean concentration $C = C_o$:

$$[x] = L \equiv \sqrt{\gamma_o/(\rho_o g)}\ ,\ [z] = H\ ,\ [t] = L/U\ ,$$
$$[u,w] = (U,\epsilon U)\ ,\ [\rho] = \rho_o = \rho(C_o)\ ,\ [p] = \rho_o g H\ ,$$

where L is the capillary length, $\gamma_o = \gamma(C_o)$ is the surface tension at the concentration C_o, $\epsilon = H/L \ll 1$ is the aspect ratio of the film height to the capillary length, and $U = gH^2/\nu_o$ is the characteristic velocity scale. This scaling is applied to equations (3) - (10) (see Appendix for details). The barodiffusion term is balanced with the remaining terms in the single component mass conservation equation using

$$C = C_o + \epsilon^2 c(x,z,t)\ ,\ \rho = \frac{1}{1+\epsilon^2 V c(x,z,t)}\ ,$$

which leads to the following scaled equations (the terms up to $O(\epsilon^2)$ are retained)

$$\epsilon^2 V\rho(c)\left\{c_t + uc_x + wc_z\right\} = u_x + w_z \tag{11}$$

$$0 = -\epsilon p_x + \rho(c)\sin\alpha + \left\{(\mu u_z)_z + \epsilon^2\left[(\mu u_x)_x + \frac{1}{3}\left((\mu\left(u_x + w_z\right))_x\right]\right\} \tag{12}$$

$$0 = -p_z - \rho(c)\cos\alpha + \epsilon\left\{(\mu w_z)_z + \frac{1}{3}\left(\mu\left(u_x + w_z\right)_z\right) + \epsilon^2\left(\mu w_x\right)_x\right\} \tag{13}$$

$$\epsilon\rho(c)\left[c_t + \mathbf{u}\cdot\nabla c\right] = \frac{1}{Pe}\left\{\left[\rho(c)c_z\right]_z + \beta V\left[\rho\left(p_z\right)\right]_z\right\} + \frac{\epsilon^2}{Pe}\left\{\left(\rho(c)c_x\right)_x + \beta V\left[\rho\left(p_x\right)\right]_x\right\} \tag{14}$$

Here $V = \rho_o\,(1/\rho_1 - 1/\rho_2)$ measures the difference in specific volumes of the two components, $Pe = UH/D = gH^3/(\nu_o D)$ is the Peclet number of the mixture, and $\bar{\beta} \equiv \epsilon^2\beta = \rho_o g H/(P_o)$ is the ratio of the hydrostatic pressure of the mixture to the ambient pressure. In the following we have assumed negligible inertial effects, i.e. we consider $Re = gH^3/\nu_o^2 \ll \epsilon$. However, $Pe \neq 0$, so we retain advection in the solute equation.

The rescaled boundary conditions at $z = 0$ become

$$u = w = 0 \qquad [c_z + p_z + \rho\cos\alpha] = 0 \tag{15}$$

and at the free surface, $z = h(x,t)$:

$$h_t + uh_x = w \tag{16}$$

$$(u_z + \epsilon^2 w_x)(1 - \epsilon^2 h_x^2) - 4\epsilon^2 u_x h_x = \epsilon M\,[c_x + h_x c_z]\,N\ ,$$

$$-p - \frac{2}{3}\epsilon(u_x + w_z) + \frac{2\epsilon}{N^2}\left\{w_z(1 - \epsilon^2 h_x^2) - h_x(u_z + \epsilon^2 w_x)\right\} = \left(1 + \epsilon^2 Mc\right)\frac{h_{xx}}{N^3}\ , \tag{17}$$

$$\left\{(c_z - \epsilon^2 h_x c_x) + \beta V(p_z - \epsilon^2 p_x h_x)\right\} = 0\ , \tag{18}$$

where $N = \sqrt{1 + \epsilon^2 h_x^2}$ and $M = (\gamma_1 - \gamma_2)/(\gamma_o)$ is the Marangoni parameter.[32]. Note that for glycerol and water, $V < 0$ and $M < 0$

To solve this system, we use lubrication theory. Let us assume that all of the remaining dimensionless groups are $O(1)$. We expand

$$\begin{aligned} u &= u_o + \epsilon u_1 + \epsilon^2 u_2 + \cdots \\ w &= w_o + \epsilon w_1 + \epsilon^2 w_2 + \cdots \\ c &= c_o + \epsilon c_1 + \epsilon^2 c_2 + \cdots \\ p &= p_o + \epsilon p_1 + \epsilon^2 p_2 + \cdots\ . \end{aligned}$$

The equations and boundary conditions above can be solved to find velocities, pressures and concentrations to order ϵ which are given in the Appendix. It is useful to note that the single component conservation equation becomes $c_{oz} = -\beta V p_{oz} = \beta V\cos\alpha$, which gives $c_o = z\beta V\cos\alpha + \bar{c}(x,t)$, showing that hydrostatics does indeed induce a concentration gradient in the film. Combining conservation of mass with the velocities, and using (A7) in the Appendix, with $h_t = -h^2 h_x \sin\alpha$ as a simplification, we arrive at the following equation for the evolution of the film thickness:

$$h_t + h^2 h_x \sin\alpha + \epsilon \left\{ \frac{h^3}{3} \left[h_{xxx} - \cos\alpha \, h_x \right] \right. \tag{19}$$
$$\left. + M \frac{h^2}{2} \left[\bar{c}_x + \beta V h_x \cos\alpha \right] \right\}_x = O(\epsilon^2) \; .$$

which for $\beta = 0$ reduces to the standard solutalcapillarity interfacial equation.

Equation (20) must be coupled with an evolution equation for concentration, $\bar{c}$. To find the equation of motion for the concentration $\bar{c}_1$, we need to consider equation (14) at $O(\epsilon^2)$. Integrating (14) from $z = 0$ to $z = h$ we find

$$\frac{1}{Pe} \left[c_{2z} + \beta V (p_{2z}) \right]_o^h + \frac{1}{Pe} \left[h \bar{c}_{xx} + h p_{oxx} \right] =$$
$$\int_o^h c_{1t} + u_o c_{1x} + w_o c_{1z} \, dz + \left\{ \frac{h^3}{3} \left[-p_{ox} \right] M \frac{h^2}{2} \left[\bar{c}_x + \beta V h_x \cos\alpha \right] \right\} \bar{c}_x$$

and

$$\int_0^h c_{1t} + u_o c_{1x} + w_o c_{1z} \, dz =$$
$$-\frac{7}{24} \beta V \sin^2\alpha \left[\left(h^4 h_x \right)_x \right] + \frac{Pe \, \beta V \sin^2\alpha \cos\alpha}{3024} \left\{ 2h^7 h_{xx} - 161 h^6 h_x^2 \right\}$$
$$- \frac{Pe \sin^2\alpha}{7560} \left\{ 121 h^7 \bar{c}_{xx} - 238 h^6 h_x \bar{c}_x \right\} \; . \tag{20}$$

A discussion of the different terms in equation (20) is useful here. The first term on the RHS corresponds to the barodiffusion component, resulting from the $w_o c_{1z}$ term. The second term corresponds to the advection induced by the inhomogeneous term in (A6). The final, stabilizing term arises from Taylor dispersion in a nonuniform film with zero shear stress along the free surface. Note that these effects are acting only in the x-direction and are due to the presence of the base-state flow. To extend this study to higher dimensions, we note that capillarity, solutalcapillarity and Fickian diffusion are isotropic processes, and the gradient terms in (20) for these processes are represented by ∇ in the three-dimensional extension below (analagous to a similar extension of a Benney formulation of a single component thin film to three dimensions found in [30]). Further, we collect the $\bar{c}_1$ terms with the $\bar{c}$ terms (i.e. $c = \bar{c} + \epsilon \bar{c}_1$) at leading order. Finally, we find the final depth averaged governing equations for film thickness and concentration:

$$h_t + h^2 h_x \sin\alpha + \epsilon\nabla\cdot\left\{\left[\frac{h^3}{3}\nabla\left[\nabla^2 h - \cos\alpha\, h\right] + M\frac{h^2}{2}\nabla\left[c + \beta V h\cos\alpha\right]\right]\right\} = 0 \qquad (21)$$

$$\begin{aligned} c_t + \frac{h^2}{3}\sin\alpha c_x - \frac{\beta V h^2 h_x \sin 2\alpha}{12} \;=\; & -\epsilon\left\{\frac{h^2}{3}\nabla\left[\nabla^2 h - h\cos\alpha\right] + M\frac{h}{2}\nabla\left[c + \beta V h\cos\alpha\right]\right\}\cdot\nabla c + \\ & \underbrace{\epsilon\frac{Pe\sin^2\alpha}{7560}\left\{121h^6 c_{xx} - 238h^5 h_x c_x\right\}}_{\text{Taylor dispersion}} + \epsilon\frac{7\beta V\sin^2\alpha}{24}\left\{h^3 h_{xx} + 4h^2 h_x^2\right\} \\ & -\epsilon\frac{Pe\,\beta V\sin^2\alpha\cos\alpha}{3024}\left\{2h^6 h_{xx} - 161h^5 h_x^2\right\} \\ & \underbrace{+\frac{\epsilon}{hPe}\nabla\cdot\left\{h\nabla c + \beta V\left[h\nabla p_o\right]\right\}}_{\text{Fickian diffusion}} \end{aligned} \qquad (22)$$

Dimensionless Parameter	Definition	Experimental Range
ϵ	H/L	1/100
Re	gH^3/ν_2	10^{-4}
Pe	$gH^3/(\nu_2 D)$	100-500
β	$\rho_o g L^2/(P_o H)$	1-10
V	$\rho_o\left(\rho_2-\rho_1\right)/((\rho_1\rho_2)$	$-1/5$
M	$\left(\gamma_2-\gamma_1\right)/\gamma_o$	-1

TABLE II: Table of dimensionless variables

IV. LINEAR STABILITY THEORY

We consider the linear stability of the exact solution to (21), (22), $h = 1$ and $c = 0$, using a standard normal-mode analysis. Assume a deviation of this base state of the form

$$\begin{pmatrix} h(x,y,t) \\ c(x,y,t) \end{pmatrix} \;=\; \begin{pmatrix} 1 \\ 0 \end{pmatrix} + \delta\begin{pmatrix} \hat{H} \\ \hat{C} \end{pmatrix} e^{\sigma t + i\mathbf{k}\cdot\mathbf{x}}\;, \qquad (23)$$

where $\delta \ll 1$ is an infinitesimally small amplitude, σ is the growth rate of the disturbance, $\mathbf{k} = (k_x, k_y)$ is the wavenumber vector, and $\mathbf{x} = (x, y)$ is the spatial location along the plate. We assume disturbances that are $2\pi-$periodic in both x and y.

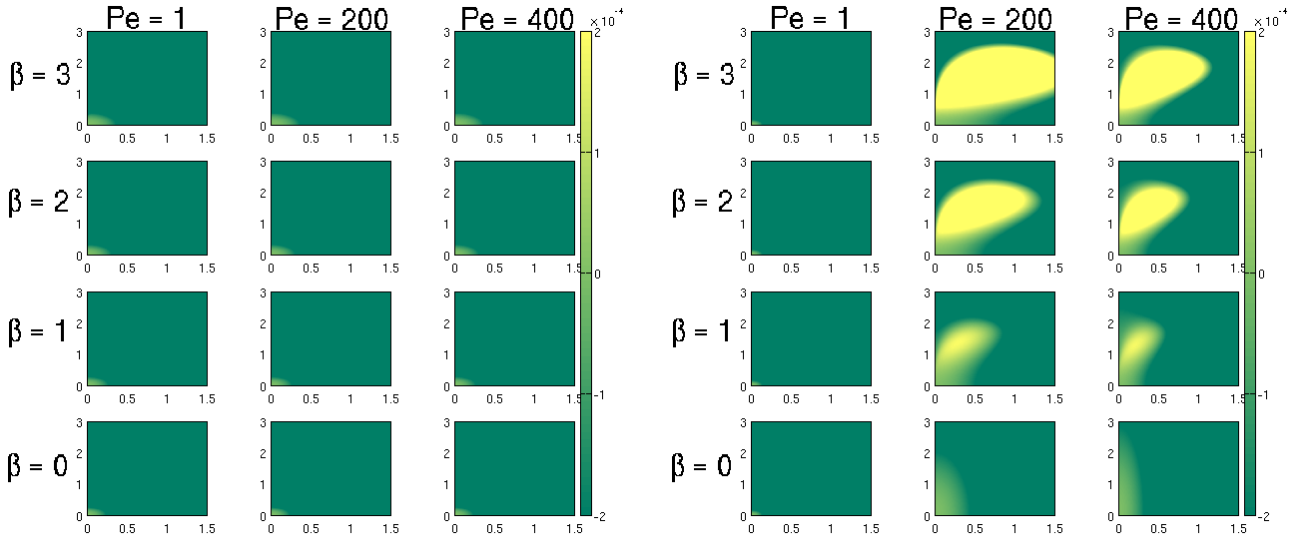

(a) (b)

FIG. 6: Contour plot of (a) the real part of the growth rate for the interfacial mode $\mathrm{Re}\{\sigma_h\}$ and of (b) the concentration mode $\mathrm{Re}\{\sigma_c\}$ for $\beta = 0, 1, 2, 3$ and $Pe = 1, 200, 400$. The x- and y axes correspond to the the x- and y component of the wavevector, respectively. Note that $M = -1, V = -0.2, \alpha = 10°$, and $Re = 0$.

Applying the form (23) to the system of equations (21), (22) and keeping only terms that are linear in δ leads to the following algebraic system

$$\begin{pmatrix} \sigma + ia_{11} + \epsilon b_{11} & \epsilon b_{12} \\ \beta V \left\{ ia_{21} + \epsilon b_{21} \right\} & \sigma + \frac{i}{3} a_{11} + \epsilon b_{22} \end{pmatrix} \begin{pmatrix} \hat{H} \\ \hat{C} \end{pmatrix} = \begin{pmatrix} 0 \\ 0 \end{pmatrix} \tag{24}$$

where the coefficents $a_{11}, b_{12}, b_{21}, b_{22}$ are given by

$$\begin{aligned} a_{11} &= k_x \sin\alpha \\ b_{11} &= \left\{ |\mathbf{k}|^2 \left[\left(\frac{1}{3} - \frac{\beta V M}{2} \right) \cos\alpha + \frac{|\mathbf{k}|^2}{3} \right] \right\} \\ b_{12} &= -\frac{M}{2} |\mathbf{k}|^2 \\ a_{21} &= -\frac{k_x \sin 2\alpha}{12} \\ b_{21} &= \left\{ \frac{7}{24} k_x^2 \sin^2\alpha - \frac{Pe\, k_x^2 \sin^2\alpha \cos\alpha}{1512} + \frac{|\mathbf{k}|^2 \left(\cos\alpha + |\mathbf{k}|^2 \right)}{Pe} \right\} \\ b_{22} &= \left\{ \frac{121}{7560} Pe k_x^2 \sin^2\alpha + \frac{|\mathbf{k}|^2}{Pe} \right\} . \end{aligned}$$

Note that all of these coefficients are positive except b_{21}, which represents the competition between linear barodiffusive effects and the advective terms induced by the flow and the concentration gradient in z.

To find the dispersion relation, we set the determinant of the matrix in (24) to zero, and find the growth rates σ. It is instructive, however, to consider first the case with no barodiffusion, namely, $\beta = 0$. In this case, the system (24) is upper triangular, and the growth rates are given by the requirement that the diagonal elements vanish

$$\sigma_{oh} = -\epsilon \left\{ |\mathbf{k}|^2 \left[\left(\frac{1}{3} - \frac{\beta V M}{2} \right) \cos\alpha + \frac{|\mathbf{k}|^2}{3} \right] \right\} - i k_x \sin\alpha \tag{25}$$

$$\sigma_{oc} = -\epsilon \left\{ \frac{121}{7560} Pe k_x^2 \sin^2\alpha + \frac{|\mathbf{k}|^2}{Pe} \right\} - \frac{i\, k_x \sin\alpha}{3} \ . \tag{26}$$

Equation (25) is the standard dispersion relation for a single-phase film falling down an inclined plane [5]. Since inertial effects are neglected, this mode remains stable. Similarly, (26) reflects stability through both Fickian diffusion and Taylor dispersion. Thus the interfacial growth rate σ_{oh} evolves independently of the solutal concentration σ_{oc}.

Let σ_h and σ_c correspond to the growth rates of the interfacial and of the concentration mode, respectively. Consider the case when β is small, and assume that $\sigma_c = \sigma_{oc} + \beta\sigma_{1c} + \cdots$. If we then solve for the real part of σ_{1c} through an asymptotic expansion of the dispersion relation for small β, we find that

$$\begin{aligned} \mathrm{Re}(\sigma_{1c}) &= \frac{V\, b_{12}}{\sigma_{oc} - \sigma_{oh}} \{ i a_{21} + \epsilon b_{21} \} \\ &= \epsilon \frac{|\mathbf{k}|^2 MV}{2|\sigma_{oc} - \sigma_{oh}|^2} \left\{ \frac{1}{18} k_x^2 \sin\alpha \, \sin 2\alpha + O(\epsilon^2) \right\} \ . \end{aligned}$$

Since $M < 0, V < 0$, the real part of σ_1 is positive; if we are near the solutal stability criterion, $\sigma_{oc} \approx 0$, the mode of instability will depend on the solutalcapillarity effect M between the two components of the mixture Note that this instability is not present if the components have equal density ($V = 0$). Thus, if σ_{oc} is small, with $Pe \gg 1$ and $k_x \ll 1$ for example, then barodiffusion can act with solutalcapillarity to induce an instability. This régime corresponds to the case when both Taylor dispersion and Fickian diffusion effects are small. Note that the eigenvector associated with σ_c, $(\hat{H}_c, \hat{C}_c)$, has a component for which $\hat{H}_c \neq 0$. Hence, even though the instability arises due to changes in the concentration field, the interfacial response need not be zero.

For values of $\beta MV > 2/3$, the interfacial equation (21) becomes ill-posed, and any results from the model in this régime are considered to be unphysical. Since we know the values of M and V from the experiment, we use this bound to determine an upper-bound for β.

We explore how the wavenumber of the maximum growth rate varies with Pe and with β. In Figure 6 we show the real part of the growth rate of the disturbance for the interfacial mode σ_h (a) and for the concentration mode σ_c (b). Each subfigure corresponds to a contour plot with $0 \leq k_x \leq 3/2$ and $0 \leq k_y \leq 3$. We keep V, M fixed as in Table II. The colors correspond to the growth rate, with (dark) green being stable, (grey) yellow-green being neutrally stable, and (light) yellow being more unstable. Note that the interfacial mode remains stable for all of the values of β and Pe considered, and the stability behavior is not sensitive to these parameters.

However, the concentration mode shown in Figure 6(b) does depend on the values of β and Pe. For $\beta = 0$, we note that the stability in the x-direction is enhanced by Taylor dispersion as Pe increases. Increasing Pe reduces the effect of Fickian diffusion, leading to the elliptical contours found for $Pe = 400$. As the barodiffusion coefficent β increases, a mode of instability develops for sufficiently high Pe. The wavevector of the disturbance is oblique to the flow. Due to the symmetry in the y-coordinate, this leads to unstable disturbances which may become unstable. One example of such a superposition is given in Figure 7. Note that the interfacial deflection (shown by the meshed surface) is deformed in a different pattern than is seen in the concentration field shown with the color contour plot along the $z = 0$ axis.

To confirm our understanding of the physical onset of this instability, we explore how the wavenumber of the maximum growth rate varies with Pe and β. We consider $\beta = 1, 2, 3$ and note that the stability depends on the product βVM. Hence the instability does not occur for mixtures which have the same density, even if soluable surface acting agents are present. Figure 8a shows how the growth rate varies with Pe for $\beta = 1, 2, 3$. Notice that the instability is present for $Pe > Pe_c = 41$ for $\beta = 1$, and for $Pe > Pe_c = 15$ for $\beta = 3$. In Figure 8b, we show the locus of wavenumbers for the mode with the maximal growth rate. As $Pe \to Pe_c$, the wavenumber of the maximally growing mode approaches the origin in this plane.

Figure 9 shows the influence of the inclination angle α on the stability properties. From Fig. 9a, we note that the instability vanishes for sufficiently large angles. The angle at which

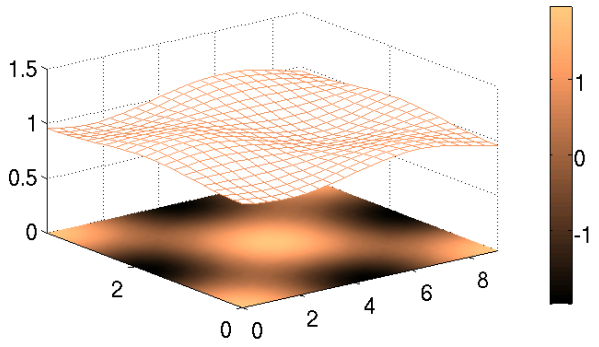

FIG. 7: Physical shape of the sum of two oblique waves $(k_x, \pm k_y)$ for the unstable concentration mode. The interfacial shape is shown in the surface plot (lines), while the concentration field is displayed in the contour plot along the $z = 0$ plane. $V = -0.2, M = -1, Pe = 200, \beta = 3$.

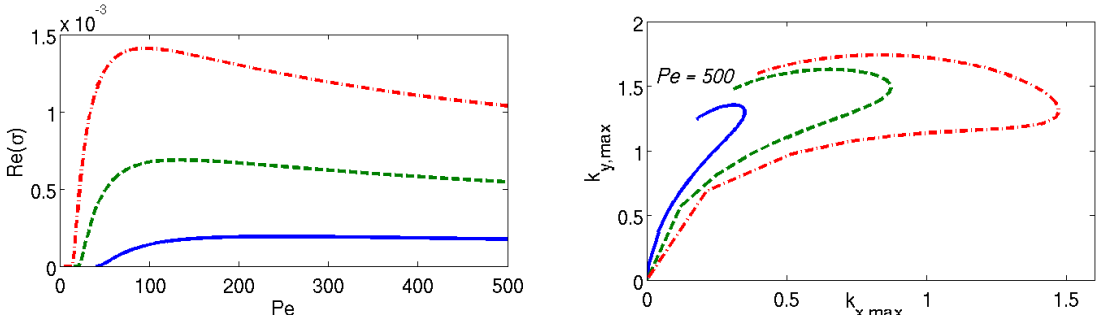

(a) (b)

FIG. 8: (a) Growth rate of concentration mode as a function of Pe for $V = -0.2, M = -1, Re = 0, \alpha = 10^\circ$ for $\beta = 1$ (solid curve), $\beta = 2$ (dashed curve), and $\beta = 3$ (dashed-dot curve). Note that the mode becomes unstable for $Pe > Pe_c$. (b) Wavenumber locus $(k_{x,max}, k_{y,max})$ for maximally growing concentration mode as a parametric function of Pe for $\beta = 1, 2, 3$.

this mode restabilizes increases for larger values of β. For sufficiently small values of α, we see that the instability becomes two-dimensional, as can be seen in Figs. 9c and 9d. Notice that near this region, we can find angles at which the wavelengths in the x and y direction are comparable. Finally, we note that as $\alpha \to \pi/2$, the x-component of the wavenumber becomes quite small compared the y-component. We speculate that the disparate aspect ratio of the elliptical form of the instability may play a role in the formation of rivulets in multi-component films.

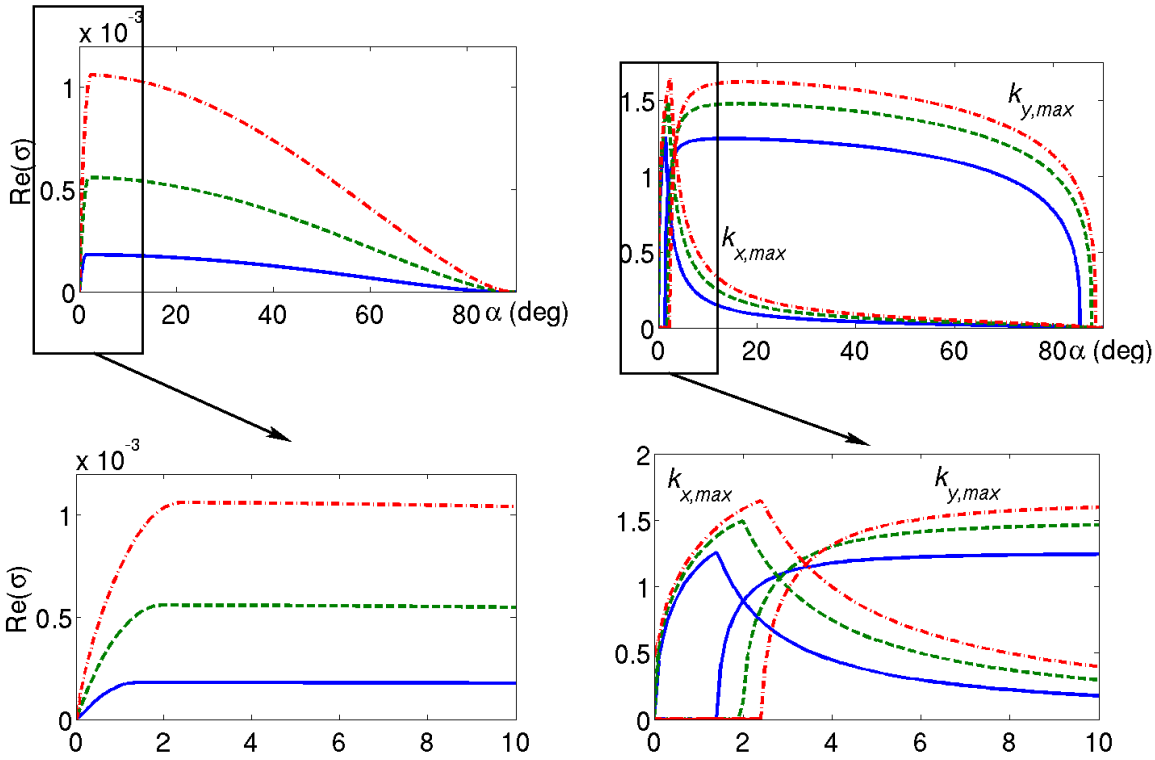

(a) (b)

FIG. 9: (a) Growth rate of concentration mode as a function of α for $Pe = 500, V = -0.2, M = -1, Re = 0$ and $\beta = 1$ (solid curve), $\beta = 2$ (dashed curve), and $\beta = 3$ (dashed-dot curve). (b) Wavenumber for maximally growing concentration mode as a function of α. Note that the curves which are larger for $\alpha > 20°$ correspond to $k_{y,max}$, while the lower curves in this region correspond to $k_{x,max}$.

V. CONCLUSIONS

A. Comparison with experiments

The linear stability analysis of the long-wave model (21, 22) has several features which appear in the experiments. Firstly, we note that the instability appears only for $\beta \neq 0$, and appears to grow more quickly with increasing β. This is consistent with the appearence of dimples in Figure 5. Due to the hydrostatics of the *reservoir*, vertical concentration gradients near the inlet are an order of magnitude larger than those in the film further down the pitch. In addition, the interfacial thickness near the entrance to the pitch grows

downstream since the flow rate from the reservoir exceeds the flow rate under the gate. Since the vertical velocity is proportional to h_x, and the instability is proportional to β, the linear stability theory presented above predicts an unstable film near the inlet. This result is consistent with the localization of the dimples near the inlet of the film. We expect that the instability enhances mixing of the solution, resulting in a restabilization of the film, with vertical concentration gradients dictated by the mean film thickness.

Secondly, the growth rates predicted in the model are on the order of $10^{-4} - 10^{-3}$ in dimensionless form. This suggests growth times scales on the order of $10^3 - 10^4$. Our time scale $L/U \approx 30\,\mathrm{s}$, if we use $\epsilon = 0.01$ as above. Thus, the time for an observable instability are quite long. However, the characteristic speed of the concentration mode $U/3 \approx 30\mu\mathrm{m/s}$, which translates to an instability occurring within 1 m down the pitch. This is again on the same order of magnitude as the experiment if we consider the dimples that appear far from the inlet (see the boxed region in Figure 5).

Thirdly, we note that the initial disturbance shown in Figure 3 evolves to an elliptical shape with the streamwise wavelength $L_x > L_y$. This corresponds qualitatively to the linear stability theory where $k_x < k_y$. Note that the capillary length scale for our system is around 3 mm, so the dimensional lengths shown in Figure 7 correspond to $L_x \approx 2.5\,\mathrm{cm}$ and $L_y \approx 9\,\mathrm{mm}$. Again, the experimental data shown in Figure 3 (second frame) appear consistent with our model.

B. Discussion

An isotropic instability for thin binary fluid mixtures flowing down an inclined plane under isothermal conditions is reported. The instability occurs owing to pressure gradients which drive mass fluxes. If the components of the mixture have different densities ($V \neq 0$), these component fluxes are not equal, driving segregation and hence, gradients in concentration. Furthermore, if the two components have different surface tensions ($M \neq 0$), gradients in concentration will lead to Marangoni convection. The instability may be enhanced by the presence of a glycerol-soluble surface reagent that is present in the manufacture of glycerol.

We propose a model based on solutalcapillarity and barodiffusion of binary mixtures valid in a long-wave régime. A linear stability analysis of this model lends insight into the onset of the instability observed in the experiment over a wide range of parameter values. The key

aspects of the instability require that both Fickian diffusion and Taylor dispersion are small, the component fluids have different surface tension and bulk densities, and that concentration gradients on the scale of barodiffusive effects are present. Large Peclet numbers and long-waves mitigate Fickian diffusion and Taylor dispersion hence, advection is necessary for the instability to occur.

Although we have identified a potential mechanism for the onset of dimples, the form of the dispersion relation suggests that different physical mechanisms could yield a similar instability. For example, the adsorption of water by glycerol may also play a role in developing concentration gradients of glycerol perpendicular to the plane. The presence of this vertical concentration gradient, regardless of how it is generated, is key for the onset of the instability. In our model, barodiffusion is the mechanism which drives the formation of this gradient. Other possible mechanisms, such as evaporation or the presence of impurtities could also set up a response that corresponds to dimples. The possiblity that impurities are instigating the instability would suggest that the observerations correspond to a response to a finite-amplitude disturbance of the film. We leave analyses of this sort for future work.

---

[1] P.L. Kapitza and S.P. Kaptiza, "Wave flow of thin viscous fluid layers", *Zh. Eksp. Teor. Fiz*, **18** 3-28: (1948).

[2] P.L. Kaptiza and S.P. Kaptiza, "Wave flow of thin fluid layers of liquid", *Zh. Eksp. Teor. Fiz*, **19** 105-120: (1949).

[3] J. Liu, J. D. Paul, and J. P. Gollub, "Measurements of the primary instabilities of film flows," J. Fluid Mech. **250** 69-101: (1993).

[4] H.-C. Chang, "Wave evolution on a falling film", *Annu. Rev. Fluid Mech.* **26** 103-136: (1994).

[5] A. Oron, S.H. Davis, and S.G. Bankoff, "Long-scale evolution of thin liquid films", *Rev. Mod. Phys.* **69** No. 3 931-980: (1997).

[6] C. Ruyer-Quil and P. Manneville, "Further accuracy and convergence results on the modeling of flows down inclined planes by weighted-residual approximations", *Phys. Fluids* **14** No. 1 170-183: (2002).

[7] O.K. Matar, "Nonlinear evolution of thin free viscous films in the presence of soluble surfactant", *Phys. Fluids* **14** No. 2 4216-4234: (2002).

[8] A. Podolny, A.A. Nepomnyashchy, and A. Oron "Marangoni convection in binary and nanofluids" *Bulletin of the 60*$^{\text{th}}$ *Annual Meeting of the Division of Fluid Dynamics*, American Physical Society, November 2007.

[9] L. Grunberg and A.H. Nissan, "Mixture law for viscosity." Nature, **164**, 799-800: (1949).

[10] C. Eckart, "The thermodynamics of irreversible processes II. Fluid mixtures", *Phys. Rev.* **58** 269-275: (1940).

[11] J.W. Cahn and J.E. Hilliard, "Free Energy of a Nonuniform System. I. Interfacial Free Energy", *J. Chem. Phys.* **28** No.2 258-267: (1958).

[12] P.C. Hohenberg and B.I. Halperin, "Theory of dynamic critical phenomena", *Rev. Mod. Phys.* **49** No. 3 435-479: (1977).

[13] V. Brandani and J.M. Prausnitz, "Two-fluid theory and thermodynamic properties of liquid mixtures: General theory", *Proc. Natl. Acad. Sci, USA* **79** 4506-4509: (1982).

[14] L.K. Antanovskii, "A phase filed model of capillarity", *Phys. Fluids* **7** No. 4 747-753: (1995).

[15] L.D. Landau & E.M. Lifshitz, *Fluid mechanics*. Oxford: Pergamon.

[16] G.I. Taylor, "Dispersion of soluble matter in solvent flowing slowly through a tube", *Proc. Roy. Soc. London A* **219** No. 1137 186-203: (1953).

[17] G.I. Taylor, "Conditions under which dispersion of a solute in a stream of solvent can be used to measure molecular diffusion", *Proc. Roy. Soc. London A* **225** No. 1163 473-477: (1954).

[18] M.P. Brenner and H.A. Stone, "Modern classical physics through the work of G.I. Taylor", *Physics Today*, **53** (5) 30-35: (2000)

[19] D.D. Joseph, "Fluid dynamics of two miscible liquids with diffusion and gradient stresses", *Eur. J. Mech B/Fluids* **9** No. 6 565-596: (1990).

[20] D.M. Anderson, G.B. McFadden, and A.A. Wheeler, "Diffuse-interface methods in fluid mechanics", *Annu. Rev. Fluid Mech.* **30** 139-165: (1998).

[21] J. Lowengrub and L. Truskinovsky, "Quasi-incompressible Cahn-Hilliard fluids and topological transitions", *Proc. R. Soc. Lond. A* **454** 2617-2654: (1998).

[22] A.E. Hosoi and J.W.M. Bush, "Evaporative instabilities in climbing films", *J. Fluid Mech.* **442**, 217-239: (2001).

[23] S.E. Bechtel, M.G. Forest, F.J. Rooney, and Q. Wang, "Thermal expansion models of viscous fluids based on limits of free energy", *Phys. Fluids* **15** No. 9 2681-2693: (2003).

[24] M. Bourich, M. Hasnaoui, M. Mamou and A. Amahmid, "Soret effect inducing subcritical and

Hopf bifurcations in a shallow enclosure filled with a clear binary fluid or a saturated porous medium: A comparative study", *Phys. Fluids* **16** No. 3 551-568: (2004).

[25] A. Oron and A.A. Nepomnyashchy, "Long-wavelength thermocapillary instability with the Soret effect", *Phys. Rev. E* **69** 016313: (2004).

[26] A. Podolny, A. Oron, and A.A. Nepomnyashchy, "Long-wave Marangoni instability in a binary-liquid layer with deformable interface in the presence of Soret effect: Linear theory", *Phys. Fluids* **17** 104104: (2005).

[27] A. Podolny, A. Oron, and A.A. Nepomnyashchy, "Linear and nonlinear theory of long-wave Marangoni instability with the Soret effect at finite Biot numbers", *Phys. Fluids* **18** 054104: (2006).

[28] S. Shklyaev, A.A. Nepomnyashchy, and A. Oron, "Three-dimensional oscillatory long-wave Marangoni convection in a binary liquid layer with the Soret effect: Bifurcation analysis", *Phys. Fluids* **19** 072105: (2007).

[29] U. Thiele, S. Madruga, and L. Frastia, "Decomposition driven interface evolution for layers of binary mixtures. I. Model derivation and stratified base states", *Phys Fluids* **19** 122106: (2007).

[30] S.W. Joo and S.H. Davis, "Instabilities of three-dimensional viscous falling films", *J. Fluid Mech.* **242** 529-547: (1992).

[31] The results presented here were not sensitive to gate height and dimples were observed for a variety of film thicknesses.

[32] Due to our choice of the capillary length scale, the Marangoni number measures the relative difference in bulk surface tensions compared to the mixture value.

Appendix A: Rescaled Equations

In this appendix, we present the nondimensionalized equations and derive the lowest and first order velocity, pressure and concentration fields. After applying the scaling and nondimensionalizing the equations of motion, we find that equations (3) - (5) become

$$V\rho(C)\left\{C_t + uC_x + wC_z\right\} = u_x + w_z \tag{A1}$$

$$\epsilon\rho(C)\,Re\left\{u_t + uu_x + wu_z\right\} = -\epsilon p_x + \rho(C)\sin\alpha + \left\{(\mu u_z)_z + \epsilon^2\left[(\mu u_x)_x + \frac{1}{3}\left((\mu\left(u_x + w_z\right)\right)_x\right]\right\} \tag{A2}$$

$$\epsilon^2\rho(C)Re\left\{w_t + uw_x + ww_z\right\} = -p_z - \rho(C)\cos\alpha + \epsilon\left\{(\mu w_z)_z + \frac{1}{3}\left(\mu\left(u_x + w_z\right)_z\right) + \epsilon^2\left(\mu w_x\right)_x\right\} \tag{A3}$$

$$\epsilon\rho(C)\left[C_t + \mathbf{u}\cdot\nabla C\right] = \frac{1}{Pe}\left\{\left[\rho(C)C_z\right]_z + \epsilon\bar{\beta}V\left[\rho\left(p_z\right)\right]_z\right\} + \frac{\epsilon^2}{Pe}\left\{\left(\rho(C)C_x\right)_x + \bar{\beta}V\left(\rho\left(p_x\right)\right)_x\right\} \quad , \tag{A4}$$

At leading order, we find from (13) and (14) that

$$p_{oz} = -\cos\alpha \ , \ c_{ozz} + \beta V p_{ozz} = 0 \ .$$

Since there is no mass flux through the plate $z = 0$ or through the interface, we can integrate the conservation of concentration equation once to find

$$c_{oz} = -\beta V p_{oz} = \beta V\cos\alpha \ ,$$

which gives $c_o = z\beta V\cos\alpha + \bar{c}(x,t)$. From the normal stress condition (17) the leading-order pressure is of the form

$$p_o(x,z,t) = (h - z)\cos\alpha - h_{xx} \ .$$

The leading-order contribution from (12) gives

$$u_o(x,z,t) = -\sin\alpha\frac{z}{2}\left(z - 2h\right) \ .$$

From conservation of mass (11), we find that

$$w_o = -\frac{z^2}{2}\left(h_x\sin\alpha\right) \ .$$

At $O(\epsilon)$, we find the following equations from (14)

$$\frac{1}{Pe}\left[c_{1z}+\beta V p_{1z}\right]\Big|_o^h \;=\; \int_o^h \bar{c}_t + u_o\bar{c}_x + w_o c_{oz}\, dz \;, \tag{A5}$$

which, to conserve mass at $z=0$ and $z=h$, require

$$\bar{c}_t + \left[\frac{h^2}{3}(\sin\alpha)\right]\bar{c}_x \;=\; \frac{1}{12}h^2 h_x \beta\, V\, \sin 2\alpha \;. \tag{A6}$$

Note in addition that the kinematic boundary condition becomes

$$h_t + h^2 h_x \sin\alpha = O(\epsilon) \;, \tag{A7}$$

which we shall use below to simplify the next-order corrections. To find the correction to the concentration, vertical momentum conservation requires that $p_z = w_{1zz} = -\sin\alpha h_x$, which gives

$$\frac{1}{Pe}\,c_{1z} = \frac{\beta V h_x}{Pe}\sin\alpha + \left\{\sin\alpha\left[\frac{z^2 h}{2} - \frac{z h^2}{3} - \frac{z^3}{6}\right]\right\}\bar{c}_x + \frac{\beta V \sin 2\alpha h_x}{12}\left(h^2 z - z^3\right) \;,$$

so,

$$c_1 = \bar{c}_1(x,t) + \beta V h_x \sin\alpha\, z - \frac{Pe\,\sin\alpha}{24}\left[z(z-2h)\right]^2\,\bar{c}_x + \frac{\beta V \sin 2\alpha h_x}{24}\left[h^2 z^2 - \frac{z^4}{2}\right] \;. \tag{A8}$$

From the $O(\epsilon)$ correction term to the x-momentum equation (12) we find that

$$u_1 \;=\; (p_{ox})\,\frac{z(z-2h)}{2} + Mz\left[\bar{c}_x + \beta V h_x \cos\alpha\right] \;. \tag{A9}$$

Note that the conservation of mass equation (11) is used to find w_1, which includes variations of c with respect to time

$$w_1 \;=\; -\left[p_{oxx}\right]\frac{z^3}{6} + \left[h p_{ox}\right]_x \frac{z^2}{2} - M\bar{c}_{xx}\frac{z^2}{2} \;. \tag{A10}$$